

Conversation from anti-ferromagnetic MnBr_2 to ferromagnetic Mn_3Br_8 monolayer with large MAE

Yan Hu

Northwestern Polytechnical University

Shuo Jin

Northwestern Polytechnical University

Zhifen Luo

Northwestern Polytechnical University

Hanghang Zeng

Northwestern Polytechnical University

Jiahui Wang

Northwestern Polytechnical University

Xiao-Li Fan (✉ xfan@nwpu.edu.cn)

Northwestern Polytechnical University <https://orcid.org/0000-0002-5291-0706>

Nano Express

Keywords: 77K, MAE, MCE, MnBr_2 , two-dimensional, liquid-Nitrogen temperature

Posted Date: January 13th, 2021

DOI: <https://doi.org/10.21203/rs.3.rs-143391/v1>

License:  This work is licensed under a Creative Commons Attribution 4.0 International License.

[Read Full License](#)

Dear Editor:

We would like to submit the enclosed manuscript entitled “Conversation from anti-ferromagnetic MnBr₂ to ferromagnetic Mn₃Br₈ monolayer with large MAE”, which we wish to be considered for publication in the *Nanoscale Research Letters*. This manuscript is approved by all authors for publication. We would like to declare that the work described is original research that has not been published previously, and not under consideration for publication elsewhere, in whole or in part.

2D magnets with Curie temperature higher than liquid-nitrogen temperature (77K), large magnetic moment, and large magnetic anisotropy energy (MAE) are highly desirable in spintronics. We design Mn₃Br₈ monolayer via inducing Mn vacancy at 1/4 population in MnBr₂ monolayer which is antiferromagnetic with large magnetic moment of 5 μ_B for each Mn atom. Such defective configuration is designed to change the coordination structure of the Mn-d⁵, to achieve ferromagnetism with large magnetic moment and large MAE. Our calculations show that Mn₃Br₈ monolayer is a FM half-metal and has Curie temperature higher than 77K, large MAE of -2.33meV per formula unit. Plus, each Mn atom has large atomic magnetic moment of 13/3 μ_B . Additionally, Mn₃Br₈ monolayer maintains to be FM under small biaxial strain. Both biaxial strain and carrier doping make the MAE increase. Our designed defective structure of MnBr₂ monolayer provides a simple but effective way to achieve ferromagnetism with large MAE and large magnetic moment.

We believe our paper may be particularly interest to the readers of *Nanoscale Research Letters*.

Thank you very much for your consideration.

Yours sincerely,

Xiaoli Fan

School of Materials Science and Engineering, Northwestern Polytechnical University

Conversation from anti-ferromagnetic MnBr_2 to ferromagnetic Mn_3Br_8 monolayer with large MAE

Y. Hu,¹ S. Jin,² Z. F. Luo,¹ H. H. Zeng,¹ J. H. Wang¹, X.L. Fan^{1}*

¹ State Key Laboratory of Solidification Processing, Center for advanced lubrication and seal Materials, School of Material Science and Engineering, Northwestern Polytechnical University, 127 YouYi Western Road, Xi'an, Shaanxi 710072, China

² Queen Mary University of London Engineering School, Northwestern Polytechnical University, 127 YouYi Western Road, Xi'an, Shaanxi 710072, China

Abstract

A pressing need in low energy spintronics is two-dimensional (2D) ferromagnets with Curie temperature above the liquid-Nitrogen temperature (77K), sizeable magnetic anisotropy. We studied Mn_3Br_8 monolayer which is obtained via inducing Mn vacancy at 1/4 population in MnBr_2 monolayer. Such defective configuration is designed to change the coordination structure of the Mn-d^5 , to achieve ferromagnetism with sizeable magnetic anisotropy energy (MAE). Our calculations show that Mn_3Br_8 monolayer is a ferromagnetic (FM) half-metal and has Curie temperature of 130K, large MAE of -2.33meV per formula unit, atomic magnetic moment of $13/3\mu_B$. Additionally, Mn_3Br_8 monolayer maintains to be FM under small biaxial strain, whose Curie temperature under 5% compressive strain is 160K. Additionally, both biaxial strain and carrier doping make the MAE increase, which mainly contributed by the magneto-crystalline anisotropy energy (MCE). Our designed defective structure of MnBr_2 monolayer provides a simple but effective way to achieve ferromagnetism with large MAE in 2D materials.

1. Introduction

Spintronics exploiting the electron spin and the associated magnetic moment, has attracted extensive attention during the past few decades [1], because of its unique advantages over charge-based devices. Recently, the discovery of two-dimensional (2D) ferromagnets with long-range magnetic ordering at finite temperature [2,3] are of great significance for nanoscale spintronics and related applications, which inspires tremendous efforts in investigations and fabrications of 2D ferromagnets [4-9].

The first two 2D FM materials with atomic-thickness was achieved in 2017, that are monolayer CrI₃ [2] and bilayer Cr₂Ge₂Te₆ [3]. Unfortunately, both their Curie temperature are lower than the liquid-nitrogen temperature (77K), which limits their realistic applications. Besides the Curie temperature, sizeable magnetic anisotropy and magnetic moment are also indispensable for practical application. Large magnetic anisotropy energy (MAE) implies the benefit for the magnetic ordering against the heat fluctuation, and the possibility to reduce the grain size per bit of information; small MAE may result in super-paramagnetic rather than ferromagnetic. Large magnetic moment provides higher sensitivity, higher efficiency, and higher density for spintronics. Heavy elements are more likely to bring in large MAE due to their strong SOC effect [10]. A series of 2D FM materials composed of heavy elements have been predicted having large MAE, such as CrI₃ [11], CrAs [12], CrSeI [13], CrSiTe₃ [14], CrWI₆ [15], FeBr₂ and FeI₂ monolayers [16]. Additionally, the local magnetic moment on Mn atom of MXenes Mn₂NF₂ and Mn₂N(OH)₂ is 4.5 μ _B per Mn atom [17], which is the largest reported for FM 2D materials.

Since CrI₃ monolayer has been synthesized, transition-metal halides have attracted much attentions [18-27]. Particularly, spin Seebeck effect has been observed in bilayer MnF₂ [20]; few layers of CrI₃ has been implemented into the magnetic tunneling junctions (MTJ), demonstrating ultrahigh magnetoresistance even up to 1000000% [21]; NiCl₃ monolayer has been predicted to be a novel Dirac spin-gapless semiconductor (SGS) [22]. Particularly, MnBr₂ monolayer is antiferromagnetic with 0.25meV MAE along the perpendicular direction to the plane [16] based on the first-principles calculations; Mn²⁺ ions are in the d⁵ high-spin state with magnetic moment of 5 μ _B [16, 26]. These results imply the potential of MnBr₂ as monolayer ferromagnet with large magnetic moment. The key problem is how to convert the AFM coupling Mn ions into FM coupling.

Significant density of Mn vacancy was observed experimentally in LaMnO₃ thin films [28], and the concentration of defects can be controlled by regulating the synthesis process deliberately via irradiation of high energy particles, or chemical etching [29]. In this context, we designed the Mn₃Br₈ monolayer by inducing single Mn vacancy to MnBr₂ monolayers. Mn vacancy will change the coordination structure of the Mn atom, and break the d⁵ configuration, which may convert the anti-ferromagnetic coupling into ferromagnetic coupling and bring in large MAE due to the heavy Br atom. As we expect, Mn₃Br₈ monolayer is FM and has large MAE of -2.33 meV per formula unit, the magnetic moment for each Mn atom is 13/3 μ _B. Considering the easy introducing of strain via bending flexible substrates [30-33], elongating elastic substrate [33-35], exploiting the thermal expansion mismatch [33,36], and so on [33], and the effective control on the spin polarization of

2D materials via electrostatic doping [37,38], we also studied the Mn_3Br_8 monolayer under biaxial strain and carrier doping. Our results show that Mn_3Br_8 monolayer maintains to be FM with Curie temperature increasing under small biaxial strain. Plus, both biaxial strain and carrier doping make the MAE increase.

2. Computational methods

All the calculations in the present study were performed by adopting the spin-polarized density function theory (DFT) method as implemented in the Vienna *ab-initio* simulation package (VASP) [39]. Interactions between electrons and nuclei were described by the projector augmented wave (PAW) method [40,41], and the electronic exchange-correlation interactions were described by the Perdew-Burke-Ernzerhof (PBE) functional within the generalized gradient approximation (GGA) method [42]. The Hubbard U terms were adopted to calculate the strong-correlated interaction [43]; an effective on-site coulomb interaction parameter (U) of 4eV and an exchange energy (J) of 1eV which was adopted for studying Mn-incorporated 2D materials were used for the Mn-d electrons [44]. The Brillouin zone integration was carried out by $9\times 9\times 1$ k-mesh based on the Monkhorst-Pack scheme [45]. The phonon spectrums were calculated using the Phonopy code [46] which is implemented within the VASP package. A vacuum space of 20\AA was added along the direction perpendicular to the surface of the monolayer to avoid the interaction between the adjacent layers. The cutoff energy for the plane wave basis set was set as 500eV. The convergence criterion for the total energy and force were set as 1×10^{-6} eV and 0.01 eV/ \AA , respectively.

3. Results and discussions

3.1 Cleavage energy, ground state, and stability of the MnBr_2 monolayer

The optimized lattice constants of bulk MnBr_2 are $a=b=3.95\text{\AA}$, consistent with the previous experimental result ($a=b=3.87\text{\AA}$) [25]. We firstly explored the feasibility of exfoliating MnBr_2 monolayer from the bulk MnBr_2 . Fig. 1(a) presents the well-known, effective, and widely approved method of calculating the cleavage energy [47-49]. Specifically, the cleavage energy was obtained by calculating the variation of the total energy with respect to the separation d between the fracture parts as shown in Fig. 1(a). The interlayer long-range vdW interactions was described by the Grimme's DFT-D2 scheme [50,51]. The total energy increases with d , and then slowly converges as showing in Fig. 1(b). The calculated cleavage energy is 0.10 J/m², which is smaller compared with graphene (0.35 J/m²) [52], demonstrating the feasibility of obtaining MnBr_2 monolayer via micro-mechanical exfoliating method.

MnBr₂ monolayer has the C_{3v} symmetry as showing in Fig. 1(c); each Mn atom is surrounded by 6 neighboring Br atoms, forming an octahedral [MnBr₆]⁴⁺ unit. As showing in Fig. S1(a) and (b), three possible magnetic configurations, namely non-magnetic (NM), ferromagnetic (FM), and anti-ferromagnetic (AFM) states are considered. Our results show that the ground state of MnBr₂ monolayer is the AFM state, which is more stable than the NM and FM states by 3.91 eV and 0.9meV per formula unit, respectively. The MAE is 0.25meV, the positive value indicating that the easy magnetization axis is along the out-of-plane directions, agreeing with previous result [16]. The optimized lattice constants are a=b=3.95Å, same with the lattice constants of the bulk MnBr₂. The Mn-Br bond length is 2.73Å, and the vertical distance between the two halide planes is 3.03Å.

The stability of the MnBr₂ monolayer was further investigated by calculated the formation energy, phonon spectrum, and elastic constants. The formation energy is calculated as:

$$E_{form} = E_{MnBr_2} - E_{Mn} - 2E_{Br}$$

where E_{MnBr_2} represents the energy of MnBr₂ monolayer, E_{Mn} and E_{Br} are the energies of Mn and Br atoms in their bulk structures, respectively. The calculated E_{form} is -1.87eV per atom; the negative value means that the formation is exothermic and MnBr₂ monolayer is energetical favorable. Plus, our calculated phonon spectrum (Fig. 1(d)) for MnBr₂ monolayer shows no negative frequency in the whole Brillouin zone, indicating dynamically stable. Additionally, the calculated elastic constants (Table S1) comply with the Born-Huang criteria [53] of $C_{11} > 0$, $C_{11}C_{22} - C_{12}^2 > 0$ and $C_{66} > 0$, confirming that MnBr₂ monolayer is mechanically stable. The C_{11} and C_{22} are equal to each other, which exhibits the mechanical isotropy; the rigidity against deformation are about three times softer along the c direction comparing with that along the a or b directions. The calculated in-plane stiffness is 26.98 J/m², about 75% of the MnPSe₃ (36 J/m²) [49], and 15% of MoS₂ monolayer (180 J/m²) [54]. Plus, MnBr₂ monolayer demonstrates higher flexibility, and the ability of sustaining larger tensile strain comparing with MoS₂ monolayer (11%) [54]. This may attribute to ionic bonds for MnBr₂ monolayer against the covalent bonds of MoS₂ monolayer.

Additionally, the gravity induced out-of-plane deformation is estimated by the following equation via using the in-plane stiffness [55]:

$$\frac{h}{L} \approx \left(\frac{\rho g L}{Y_{2D}} \right)^{1/3}$$

where $\rho = 4.91 \times 10^{-6} \text{ Kg/m}^2$ is the mass density of MnBr_2 , and L is the size of the monolayer. Taking $L \approx 100 \mu\text{m}$, we obtain $\frac{h}{L} \approx 5.72 \times 10^{-4}$, which is comparable to that of monolayer CrI_3 (6.45×10^{-4}) [47], and is of the same magnitude order of graphene [55]. Our result shows that the free-standing MnBr_2 monolayer can withstand its own weight and maintain the planar structure.

The electronic band structure of MnBr_2 monolayer is shown in Fig. 1(e), which indicates that MnBr_2 monolayer is AFM semiconductor with a direct band gap of 3.35 eV. Both valence band maximum (VBM) and conduction band minimum (CBM) locate at the Γ point. To gain insight of the electronic structures, projected density of states (DOS) for the Mn-d and Br-p orbital are presented in Fig. 1(f). The five d orbitals of Mn^{2+} ion split into $a(d_{z^2})$, $e_1(d_{xz} + d_{yz})$, and $e_2(d_{xy} + d_{x^2-y^2})$ groups according to the C_{3v} symmetry, and the five d-electrons occupy the five spin-up channels of the d-orbitals. Correspondingly, Mn^{2+} ion is in the d^5 high-spin state with the magnetic moment of $5 \mu_B$. Meanwhile, the Br^{1-} ion is in the $4p^6$ low-spin state with neglectable magnetic moment (Fig. S2(a)). According to the Goodenough-Karamori-Anderson (GKA) rule, such configuration always demonstrates antiferromagnetic coupling [56].

3.2 Stability, electronic and magnetic properties of Mn_3Br_8 monolayer

Mn vacancy was introduced to break the d^5 configuration of the Mn^{2+} ions. Single Mn vacancy is introduced in the $2 \times 2 \times 1$ supercell of MnBr_2 monolayer, which gives out the Mn_3Br_8 monolayer. As showing in Fig. 2(a), each Mn atom has four nearest neighboring Mn atoms and binds to six Br atoms, forming a distorted octahedral $[\text{MnBr}_6]$ unit. Five magnetic states (NM, FM, FIM, AFM-1, and AFM-2) shown in Fig. S3 were considered. Our results indicate that the FM state is the ground state, which is more stable than the other four by 9.84 eV, 32.90 meV, 129.85 meV, and 97.65 meV per formula unit, respectively. The optimized lattice constant is still 3.95 Å. Different from MnBr_2 monolayer, Mn_3Br_8 monolayer has 2 types of Mn-Br bonds (Fig. 2(b)). The bonds between Mn atom and the two central Br atoms ($d_{\text{Mn-Br}_{1,2}}$) are 2.76 Å, while the other Mn-Br bonds ($d_{\text{Mn-Br}_{3,4,5,6}}$) are 2.59 Å. The vertical distance between the two halide planes is 3.33 Å.

To verify the feasibility of inducing single Mn vacancy, we firstly calculated the vacancy

formation energies under different experimental conditions (See details on Page 1 of SI). As showing in Fig. 2(c), the formation energies under Mn-rich/Br-rich environment is 6.30/0.71 eV per Mn vacancy, indicating that the formation of Mn vacancy is energetically more favorable under the Br-rich environment. Indeed, the S vacancy has been experimentally achieved in MoS₂ monolayer [57], and the predicted formation energy of S vacancy in MoS₂ monolayer under the S-rich environment is 2.35eV [58]. In this context, Mn₃Br₈ monolayer is synthetically approachable. Plus, there is no negative frequency found in its phonon spectrum shown in Fig. 3(a), proving the dynamically stable. These results approve our design of introducing Mn vacancy to bring in ferromagnetism.

The ferromagnetism of Mn₃Br₈ monolayer attributes to the FM super-exchange interaction. According to the Goodenough-Kanamori-Anderson (GKA) rule [56], the super-exchange between the Mn ions is FM when the Mn-Br-Mn angle is close to 90°. In such configuration (Fig. S4), the Mn-d orbital tend to AFM couples with different orthogonal Br-p orbital, thus the indirect Mn-Mn magnetic coupling is expected to be FM. But if each Mn ion has 5 unpaired electrons, it will be AFM coupling, which is true for MnBr₂ monolayer. There are existing two different super-exchange interaction paths in Mn₃Br₈ (Fig. 2(a)), and both are FM. One involves central Br_{1,2} atoms with Mn-Br bond lengths of 2.76Å and Mn-Br-Mn angles of 87.5°; the other one involves Br_{3,4,5,6} atoms with Mn-Br bond length of 2.59Å and Mn-Br-Mn angles of 95°. Particularly, hybridized interactions between p orbitals of Br_{3,4,5,6} atoms and Mn-d orbitals are stronger than that of p-d hybridization involving Br_{1,2} atoms, as showing in Fig. 3(c), specially from -2eV to -1.4eV. While from -1.4eV to -0.9eV, p-d hybridization involving Br_{1,2} atoms are dominated.

The valence electrons of Br¹⁻ ion (4p⁶) fully occupy both spin-up and spin-down channels as showing in Fig. 3(c), correspondingly, the atomic magnetic moments of Br atoms are neglectable (Fig. S2(b)). Meanwhile, the Mn ions having 13/3 d electrons are in the high spin-state with 13/3μ_B atomic magnetic moment. For each Mn ion, 2/3 d-orbital is unoccupied; the spin-up channel of both e_1 and e_2 orbitals are partially occupied and crossing the Fermi level, resulting in half-metallicity. The half-metallic character also can be observed from the spin-resolved electronic band structure shown in Fig. 3(b). The spin-up channel is metallic, while the spin-down channel is semiconducting with the indirect band gap of 2.97eV; the VBM/CBM locates at the M/Γ point. The value of the band gap is close to those of the MnP (2.86eV) [59], MnAs (2.92eV) [59], Ni₂NO₂ (2.98eV) [60], and large enough to prevent the thermally excited spin-flip.

The magnetic orientations are determined by the magnetic anisotropy energy (MAE). The MAE of magnetic solids arises from two contributors, namely, the magneto-crystalline energy (MCE) related to the spin-orbit coupling (SOC), and the magnetic dipolar anisotropy energy (MDE) attributed by the magneto-static dipole-dipole interaction. The MDE in the 3D isotropic materials, such as bcc Fe and fcc Ni, is very small. But for low-dimensional materials composed of transition metal atoms with large magnetic moment, the MDE is not neglectable [61-63]. The MCE is defined as the difference between the magnetization energy along the in-plane (100 or 010) and out-of-plane (001) directions by taking the SOC into account. The MDE is obtained as the difference of E_d between the in-plane and out-of-plane magnetizations. E_d in atomic Rydberg units is given by [61,62]

$$E_d = \sum_{ij} \frac{2m_i m_j}{c^2} M_{ij}$$

where the speed of light, $c = 274.072$, i/j are the atomic position vectors in the unit cell, and m_i/m_j is the atomic magnetic moment (μ_B) on site i/j . The magnetic dipolar Madelung constant M_{ij} is calculated via

$$M_{ij} = \sum_R \frac{1}{|R+i+j|^3} \left\{ 1 - 3 \frac{[(R+i+j) \cdot \hat{m}_i]^2}{|R+i+j|^2} \right\}$$

where R are the lattice vectors. In a 2D material, since all the R and i are in-plane, the second term would be zero for the out-of-plane magnetization, resulting in the positive M_{ij} , while M_{ij} is negative for an in-plane magnetization [63]. Therefore, the MDE relates to the magnetic moment of transition metal, and always prefers the in-plane magnetization.

The calculated MCE for Mn_3Br_8 monolayer is -1.90meV per formula unit (Fig. 4(a)), much larger than those of bulk Fe (0.001meV per atom), and Ni (0.003meV per atom) [64], and larger than that of the Fe monolayer on Rh (111) (0.08meV per atom) [65], suggesting the thermal stability of the magnetization of the Mn_3Br_8 monolayer. The relationship between the MCE and the azimuthal angle can be described by the following equation [66]:

$$MCE(\theta) = A \cos^2(\theta) + B \cos^4(\theta)$$

where A and B are the anisotropy constants and θ is the azimuthal angle. The fitting result is shown in Figs. S5. Additionally, the evolution of MCE as the spin axis rotates through the whole space is illustrated in Fig. 4(b). MCE within the xy plane show no difference, but reaches the maximum value along the direction perpendicular to the xy plane, confirming the strong magnetic anisotropy. The MDE is -0.43meV per formula unit, and MAE (MCE+MDE) is -2.33meV per formula unit. The negative value indicates that the easy magnetization axis is along the in-plane directions. The MDE does not change the magnetic orientation, but enhance the MAE and the magnetization. Additionally, the MAE of Mn₃Br₈ monolayer is much larger than that of MnBr₂ monolayer, proving again the effectiveness of our design.

We further calculated the T_c for FM Mn₃Br₈ monolayer by performing the Monte Carlo (MC) simulations based on the Heisenberg model, which has been proven to be the effective method for predicting T_c for 2D materials [11,15,48,59,67-72]. Our estimated T_c of CrI₃ monolayer is 42K [72], agreeing well with the experimental measured value [2] and previous calculation results [15,59,67,68,70,72], which proves the accuracy of our adopted method. The spin-Hamiltonian including the nearest neighboring (NN) magnetic interaction is described as

$$H = -\sum_{i,j} JM_i M_j$$

where J is the NN magnetic exchange parameter, M_{ij} is the net magnetic moment of Mn ions, i and j stand for the NN pair of Mn ions. The magnetic coupling parameter J is calculated via the energy difference between the FM and AFM states as

$$J = \frac{E_{AFM1} - E_{FM}}{16M^2}$$

The calculated J of NN Mn ions is 1.01meV; the positive value indicates the preferring of FM coupling.

The calculated J of the NN Mn ions and the $100 \times 100 \times 1$ supercell containing 20000 magnetic moment vectors was adopted to perform the MC simulations. The simulations at each temperature lasts for 10^5 steps. Each magnetic moment vector rotates randomly in all directions. Fig. 3(d) shows the evolution of specific heat defined as $C_v = (\langle E^2 \rangle - \langle E \rangle^2) / K_B T^2$ with temperature, from which we obtained the T_c of 130 K for Mn₃Br₈ monolayer by locating the peak position of C_v , higher

than the liquid-nitrogen temperature (77 K), and T_c of CrI₃ (45K) [2] and Cr₂Ge₂Te₆ (28K) [3], CrX₃ (X=F, Cl, Br) (36~51K) [11], CrXTe₃ (X=Si, Ge) (35.7K, 57,2K) [48]. Our calculations demonstrate that the FM Mn₃Br₈ monolayer has the large MAE and Curie temperature higher than the liquid-nitrogen temperature.

3.3 Mn₃Br₈ monolayer under biaxial strain and carrier doping

Strain engineering has been proven applicable for many 2D materials, and effective to alter the structural parameters, such as the bond lengths and angles, and to tune the electronic and magnetic properties. In this context, we investigated Mn₃Br₈ monolayer under the biaxial strain ranging from -5% to 5%. It turns out that Mn₃Br₈ monolayer under biaxial strain from -5% to 5% maintains to be FM and the atomic magnetic moment hardly changes. As showing in Figs. 5(a) and (c), the angles between two Mn atoms and Br_{1,2} atoms ($\theta_{\text{Mn-Br}_{1,2}\text{-Mn}}$) are 84°-90°, which increases as the strain and gradually approaches 90°. The Mn-Br-Mn angles involving Br_{3,4,5,6} atoms ($\theta_{\text{Mn-Br}_{3,4,5,6}\text{-Mn}}$) gradually deviate from 90°, ranging from 90° to 100°. Thus, super-exchange interactions between the Mn ions mediated via different orthogonal Br-p orbital are still FM.

The Mn-Mn and Mn-Br distances all increase monotonically as the strain changing from -5% to 5%. Correspondingly, the exchange parameter under the biaxial strain presented in Fig. 6(a) decreases with the biaxial strain changing from -5% to 5% and reach the largest value (1.18meV) under -5% biaxial strain. The Curie temperature of Mn₃Br₈ monolayer under -5% biaxial strain is 160 K (Fig. 7(a)). Particularly, the Mn-Br bonds under the increasing tensile strain become longer, and the angles of Mn-Br_{3,4,5,6}-Mn deviate from 90°, which are the main reason why the FM super-exchange interaction become weaker. Consequently, the Curie temperature decreases. It is similar with CrPTe₃ and FePS₃ monolayers [73]. Additionally, the MDE decreases with the increasing strain (Fig. S7(b)); the MAE under -1% biaxial strain is the largest (-3.04meV). The -5%~5% strain does not cause large structural deformation for Mn₃Br₈ monolayer, and the morphology of its band structures hardly changes. Mn₃Br₈ monolayer keeps to be half-metallic. Both VBM and CBM in the semiconducting spin-channel move upwards slightly to the higher energy as shown in Fig. 6(c) and Figs.8; the band gap increases slowly with the increasing biaxial strain to 3.12eV under 5% biaxial strain.

Electron/hole doping always leads to VBM/CBM moving away from the Fermi level. Our calculations show that Mn₃Br₈ monolayer with -1~1e ($\sim 1.7 \times 10^{14} \text{ cm}^{-2}$) carrier doping per formula

unit is still FM; the atomic magnetic moment of each Mn ion is still $13/3\mu_B$. As showing in Figs. 5(b) and (d), with carrier doping from $-1e$ to $1e$ per formula unit, the Mn-Br-Mn angles involving Br_{3,4,5,6} atoms are about $90^\circ \sim 98^\circ$; the Mn-Br_{1,2}-Mn angles are about $88^\circ \sim 90^\circ$. The Mn-Mn and Mn-Br_{1,2} distances increase with the increasing electron doping. Mn₃Br₈ monolayer with 0.2e and 0.4e carrier doping has larger magnetic exchange parameter (Fig. 6(a)). The Curie temperature at 0.2e electron doping is largest of 140K (Fig. 7(b)). Additionally, with $-1e \sim 0.2e$ doping, the MAE is along in-plane directions; the MDE decreases with the increasing electron doping. Under 0.4e doping, the MCE turns to be positive with the value of 0.41meV per formula unit; the MAE is only 0.01meV per formula unit with taking the MDE into account (Fig. S7(a) and (b)). With 0.6e, 0.8e and 1e doping, the PMA (perpendicular magnetic anisotropy energy) is 1.70, 2.42, and 5.13 meV, respectively, large enough for spintronic applications (Fig. 6(b)).

Additionally, Mn₃Br₈ monolayer with carrier doping $-1e \sim 1e$ per formula unit maintains to be half-metal. Its band gap in the semiconducting spin-channel increases/decreases slightly with the increasing electron/hole doping as showing in Fig. 6(d); the positions of the VBM and CBM do not change. Exceptional, Mn₃Br₈ monolayer turns to be FM spin-gapless semiconductors (SGS) with the metallic spin-channel opening up a very small energy gap (0.07eV) under $-0.6e$ and $-0.8e$ hole doping; its Fermi level locates in the band gap region (Figs. 9(b) and (c)). Correspondingly, electrons may be easily excited from the valence band to the conduction band with a small input of energy, which simultaneously produces 100% spin polarized electron and hole carriers. The Curie temperature at $-0.6e$ and $-0.8e$ hole doping is 110K (Fig. 7(c) and (d)), higher than liquid-Nitrogen temperature (77K). The charge density modulation of $10^{13} \sim 10^{15} \text{cm}^{-2}$ was already achieved experimentally [74-76], in this context, our predicted properties of Mn₃Br₈ monolayer with carrier doping is also experimentally approachable.

Conclusions

In summary, the stability, electronic and magnetic properties of Mn₃Br₈ monolayer have been carefully investigated. Our results show that Mn₃Br₈ monolayer is FM half-metal with 130K Curie temperature and with 2.97eV band gap for the semiconducting spin-channel. Plus, the magnetic moment of each Mn ion is $13/3\mu_B$; the MAE is -2.33meV per formula unit. The Mn₃Br₈ monolayer is designed by inducing single Mn vacancy in the $2 \times 2 \times 1$ supercell of MnBr₂ monolayer to break the AFM coupling d^5 configuration. The feasibility of forming the Mn vacancy and the dynamical, mechanical stability of Mn₃Br₈ monolayer have been comprehensively confirmed. Additionally,

Mn₃Br₈ monolayer under biaxial strain -5% ~ 5% is still FM half-metal with 2.71~3.12eV band gap for the semiconducting spin-channel, whose Curie temperature under -5% biaxial strain is 160K. Both biaxial strain and carrier doping make the MAE increase, which turns to be perpendicular to the plane under electron doping. With 0.8e and 0.6e hole doping, Mn₃Br₈ monolayer turns to be spin-gapless semiconductor (SGS) with band gap of 0.07eV. Our calculations demonstrate Mn₃Br₈ monolayer as FM half-metal with high Curie temperature, and having large MAE and large magnetic moment, and tunable electronic and magnetic properties via applying biaxial strain and carrier doping.

Acknowledgements

This work was supported by the National key R&D Program of China (2018YFB0703800), the Natural Science Fund of Shaanxi Province for distinguished Young Scholars (2019JC-10), the Polymer Electromagnetic Functional Materials Innovation Team of Shaanxi Sanqin Scholars, and sponsored by the seed Foundation of Innovation and Creation for Graduate Students (CX2020083) in Northwestern Polytechnical University.

Compliance with ethical standards

Conflict of interest: the authors declare that they have no conflict of interest.

References

1. Fert A (2008) Nobel Lecture: Origin, development, and future of spintronics. *Rev. Mod. Phys* 80: 1517.
2. Huang B, Clark G, Navarro-Moratalla E, Klein DR, Cheng R, Seyler KL, Zhong D, Schmidgall E, McGuire MA, Cobden DH, Yao W, Xiao D, Jarillo-Herrero P, Xu X (2017) Layer-dependent ferromagnetism in a van der waals crystal down to the monolayer limit. *Nature* 546:270.
3. Gong C, Li L, Li Z, Ji H, Stern A, Xia Y, Cao T, Bao W, Wang C, Wang Y, Qiu ZQ, Cava RJ, Louie SG, Xia J, Zhang X (2017) Discovery of intrinsic ferromagnetism in two-dimensional van der waals crystals. *Nature* 546:265.
4. Gong C, Zhang X (2019) Two-dimensional magnetic crystals and emergent heterostructure devices. *Science* 363:706.
5. Lu SH, Zhou QH, Guo YL, Zhang YH, Wu YL, Wang JL (2020) Coupling a crystal graph multilayer descriptor to active learning for rapid discovery of 2D ferromagnetic

semiconductors/half-metals/metals. *Adv Mater* 32:2002658.

6. Lee JW, Ko TY, Kim JH, Bark HY, Kang B, Jung SG, Park T, Lee Z, Ryu S, Lee C (2017) Structural and optical properties of single- and few-layer magnetic semiconductor CrPS₄. *ACS Nano* 11:10935.
7. Cui FF, Zhao XX, Xu JJ, Tang B, Shang QY, Xing JP, Huan YH, Liao JH, Chen Q, Hou YL, Controlled growth and thickness-dependent conduction-type transition of 2D ferrimagnetic Cr₂S₃ semiconductors. *Adv. Mater* 32:1905896.
8. Yu S, Wang Y, Song YZ, Xia L, Yang XL, Fang H, Li QL, Li XG (2021) Hole doping induced half-metallic itinerant ferromagnetism and giant magnetoresistance in CrI₃ monolayer. *Appl Surf Sci* 535:147693.
9. Deng YJ, Yu YJ, Song YC, Zhang JZ, Wang NZ, Sun ZY, Yi YF, Wu YF, Wu SW, Zhu JY, Wang J, Chen XH, Zhang YB (2018) Gate-tunable room-temperature ferromagnetism in two-dimensional Fe₃GeTe₂. *Nature* 563:94.
10. Zhuang HL, Kent PRC, Hennig RG (2016) Strong anisotropy and magnetostriction in the two-dimensional Stoner ferromagnet Fe₃GeTe₂. *Phys Rev B* 93:134407.
11. Zhang WB, Qu Q, Zhu P, Lam CH (2015) Robust intrinsic ferromagnetism and half semiconductivity in stable two-dimensional single-layer chromium trihalides. *J Mater Chem C* 3:12457.
12. Ma AN, Wang PJ, Zhang CW (2020) Intrinsic ferromagnetism with high temperature, strong anisotropy and controllable magnetization in the CrX (X=P, As) monolayer. *Nanoscale* 12:5464.
13. Han RL, Yan JY (2020) Prediction of novel 2D intrinsic ferromagnetic materials with high Curie temperature and large perpendicular magnetic anisotropy. *J. Phys Chem C* 124:7956.
14. Zhuang HL, Xie Y, Kent PRC, Ganesh P (2015) Computational discovery of ferromagnetic semiconducting single-layer CrSnTe₃. *Phys Rev B* 92:035407.
15. Huang CX, Feng JS, Wu F, Ahmed D, Huang B, Xiang HJ, Deng KM, Kan EJ (2018) Toward Intrinsic room-temperature ferromagnetism in two-dimensional semiconductors. *J. Am. Chem. Soc* 140:11519.
16. Botana AS, Norman MR (2019) Electronic structure and magnetism of transition metal dihalides: Bulk to monolayer. *Phys Rev Mater* 3:044001.
17. Kumar H, Frey NC, Dong L, Anasori B, Gogotsi Y, Shenoy VB (2017) Tunable magnetism and transport properties in Nitride MXenes. *ACS Nano* 11:7648.
18. Lin SH, Kuo JL (2014) Towards the ionic limit of two-dimensional materials: monolayer alkaline earth and transition metal halides. *Phys Chem Chem Phys* 16:20763.
19. Kong T, Stolze K, Timmons EI, Tao J, Ni D, Guo S, Yang Z, Prozorov R, Cava RJ (2019) VI₃-

- a new layered ferromagnetic semiconductor. *Adv. Mater* 31:1808074.
20. Wu SM, Zhang W, KC A, Borisov P, Pearson JE, Jiang JS, Lederman D, Hoffmann A, Bhattacharya A (2016) Antiferromagnetic Spin Seebeck Effect. *Phys Rev Lett.* 116:097204.
 21. Kim HH, Yang B, Patel T, Sfigakis F, Li C, Tian S, Lei H, Tsen AW (2018) One Million Percent Tunnel Magnetoresistance in a Magnetic van der Waals Heterostructure. *Nano Lett* 18:4885.
 22. He JJ, Li X, Lyu P, Nachtigall P (2017) Near-room-temperature Chern insulator and Dirac spin-gapless semiconductor: nickel chloride monolayer. *Nanoscale* 9:2246.
 23. Hu H, Tong WY, Shen YH, Wan XG, Duan CG (2020) Concepts of the half-valley-metal and quantum anomalous valley Hall effect. *npj Comput Mater* 6:129.
 24. Huang CX, Du YP, Wu HP, Xiang HJ, Deng KM, Kan EJ (2018) Prediction of intrinsic ferromagnetic ferroelectricity in a transition-metal halide monolayer. *Phys Rev Lett* 120:147601.
 25. Wollan EO, Koehler WC, Wilkinson MK (1958) Neutron diffraction study of the magnetic properties of MnBr₂. *Phys Rev* 110:638.
 26. Kulish VV, Huang W (2017) Single-layer metal halides MX₂ (X=Cl, Br, I): stability and tunable magnetism from first principles and Monte Carlo simulations. *J. Mater. Chem. C* 5:8734.
 27. Hu Y, Gong YH, Zeng HH, Wang JH, Fan XL (2020) Two-dimensional stable Fe-based ferromagnetic semiconductors: FeI₃ and FeI_{1.5}Cl_{1.5} monolayers. *Phys Chem Chem Phys* 22:24506.
 28. Marozau I, Das PT, Döbeli M, Storey JG, Uribe-Laverde MA, Das S, Wang C, Rössle M, Bernhard C (2014) Influence of La and Mn vacancies on the electronic and magnetic properties of LaMnO₃ thin films grown by pulsed laser deposition. *Phys Rev B* 89:174422.
 29. Zhou W, Zou X, Najmaei S, Liu Z, Shi Y, Kong J, Lou J, Ajayan PM, Yakobson BI, Idrobo JC (2013) Intrinsic structural defects in monolayer molybdenum disulfide. *Nano Lett* 13:2615.
 30. Conley HJ, Wang B, Ziegler JI, Haglund RF, Pantelides ST, Bolotin KI (2013) Bandgap Engineering of Strained Monolayer and Bilayer MoS₂. *Nano Lett* 13:3626.
 31. He K, Poole C, Mak KF, Shan J (2013) Experimental Demonstration of Continuous Electronic Structure Tuning via Strain in Atomically Thin MoS₂. *Nano Lett* 13:2931.
 32. Wang Y, Cong C, Yang W, Shang J, Peimyoo N, Chen Y, Kang J, Huang W, Yu T (2015) Strain-induced direct–indirect bandgap transition and phonon modulation in monolayer WS₂. *Nano Res* 8:2562.
 33. Hui YY, Liu X, Jie W, Chan NY, Hao J, Hsu YT, Li LJ, Guo W, Lau SP (2013) Exceptional Tunability of Band Energy in a Compressively Strained Trilayer MoS₂ Sheet. *ACS Nano* 7:7126.
 34. Plechinger G, Gomez AG, Buscema M, Van der Zant HSJ, Steele GA, Kuc A, Heine T,

- Schüller C, Korn T (2015) Control of biaxial strain in single-layer molybdenite using local thermal expansion of the substrate. *2D Mater* 2:015006.
35. Gomez AC, Roldán R, Cappelluti E, Buscema M, Guinea F, Van der Zant HSJ, Steele GA (2013) Local Strain Engineering in Atomically Thin MoS₂. *Nano Lett.* 13:5361.
 36. Roldán R, Gomez AC, Cappelluti E, Guinea F (2015) Strain engineering in semiconducting two-dimensional crystals. *J. Phys.: Condensed Matter* 27:313201.
 37. Wang Z, Zhang TY, Ding M, Dong BJ, Li YX, Chen ML, Li XX, Huang JQ, Wang HW, Zhao XT, Li Y, Chen D, Yang T, Zhang J, Ono SP, Han Z, Zhang ZD (2018) Electric-field control of magnetism in a few-layered van der Waals ferromagnetic semiconductor. *Nat Nanotech* 13:554.
 38. Jiang S, Li L, Wang Z, Mak KF, Shan J (2018) Controlling magnetism in 2D CrI₃ by electrostatic doping. *Nat Nanotech* 13:549.
 39. Kresse G, Furthmüller J (1996) Efficient iterative schemes for ab initio total-energy calculations using a plane-wave basis set. *Phys. Rev. B* 54:11169.
 40. Blöchl PE (1994) Projector augmented-wave method. *Phys Rev B* 50:17953.
 41. Kresse G, Joubert D (1999) From ultrasoft pseudopotentials to the projector augmented-wave method. *Phys Rev B* 59:1758.
 42. Perdew JP, Burke K, Ernzerhof M (1996) Generalized gradient approximation made simple. *Phys Rev Lett* 77:3865.
 43. Liechtenstein AI, Anisimov VI, Zaanen J (1995) Density-functional theory and strong interactions: Orbital ordering in Mott-Hubbard insulators. *Phys Rev B* 52:R5467.
 44. Zhou J, Sun Q (2011) Magnetism of phthalocyanine-based organometallic single porous sheet. *J. Am. Chem. Soc* 133:15113.
 45. Monkhorst HJ, Pack JD (1976) Special points for Brillouin-zone integrations. *Phys Rev B* 13:5188.
 46. Parlinski K, Li Z, Kawazoe Y (1997) First-principles determination of the soft mode in cubic ZrO₂. *Phys. Rev. Lett* 78:4063.
 47. Liu J, Sun Q, Kawazoe Y, Jena P (2016) Exfoliating biocompatible ferromagnetic Cr-trihalide monolayers. *Phys. Chem. Chem. Phys* 18:8777.
 48. Li XX, Yang JL (2014) CrXTe₃ (X = Si, Ge) nanosheets: two dimensional intrinsic ferromagnetic semiconductors. *J Mater Chem C* 2:7071.
 49. Li XX, Wu XJ, Yang JL (2014) Half-metallicity in MnPSe₃ exfoliated nanosheet with carrier doping. *J. Am. Chem. Soc* 136:11065.
 50. Grimme S (2006) Semiempirical GGA-type density functional constructed with a long-range dispersion correction. *J Comput Chem* 27:1787.

51. Bucko T, Hafner J, Lebegue S, Angyan JG (2010) Improved description of the structure of molecular and layered crystals: ab initio DFT calculations with van der Waals corrections. *J Phys Chem A* 114:11814.
52. Zacharia R, Ulbricht H, Hertel T (2004) Interlayer cohesive energy of graphite from thermal desorption of polyaromatic hydrocarbons. *Phys Rev B* 69:155406.
53. Cadelano E, Palla PL, Giordano S, Colombo L (2010) Elastic properties of hydrogenated graphene. *Phys Rev B* 82:235414.
54. Bertolazzi S, Brivio J, Kis A (2011) Stretching and Breaking of Ultrathin MoS₂. *ACS Nano* 5:9703.
55. Booth TJ, Blake P, Nair RR, Jiang D, Hill EW, Bangert U, Bleloch A, Gass M, Novoselov KS, Katsnelson MI, Geim AK (2008) Macroscopic graphene membranes and their extraordinary stiffness. *Nano Lett* 8:2442.
56. Stöhr J, Siegmann HC (2006) *Magnetism: From Fundamentals to Nanoscale Dynamics*; Springer-Verlag, New York:274.
57. Lin Z, Carvalho BR, Kahn E, Lv R, Rao R, Terrones H, Pimenta MA, Terrones M (2016) Defect engineering of two-dimensional transition-metal dichalcogenides. *2D Mater* 3:022002.
58. Liu D, Guo Y, Fang L, Robertson J (2013) Sulfur vacancies in monolayer MoS₂ and its electrical contacts. *Appl Phys Lett* 103:183113.
59. Wang B, Zhang YH, Ma L, Wu QS, Guo YL, Zhang XW, Wang JL (2019) MnX (X=P, As) monolayers: a new type of two-dimensional intrinsic room temperature ferromagnetic half-metallic material with large magnetic anisotropy. *Nanoscale* 11:4204.
60. Wang G, Liao Y (2017) Theoretical prediction of robust and intrinsic half-metallicity in Ni₂N MXene with different types of surface terminations. *Appl Surf Sci* 426:371.
61. Tung JC, Guo GY (2007) Systematic *ab initio* study of the magnetic and electronic properties of all 3d transition metal linear and zigzag nanowires. *Phys. Rev. B* 76:094413.
62. Guo GY, Temmerman W, Ebert H (1991) First-principles determination of the magnetization direction of Fe monolayer in noble metals. *J. Phys.: Condens. Matter* 3:8205.
63. Fang Y, Wu S, Zhu ZZ, Guo GY (2018) Large magneto-optical effects and magnetic anisotropy energy in two-dimensional Cr₂Ge₂Te₆. *Phys. Rev. B* 98:125416.
64. Daalderop GHO, Kelly PJ, Schuurmans MFH (1990) First-principles calculation of the magnetocrystalline anisotropy energy of iron, cobalt, and nickel. *Phys Rev B* 41:11919.
65. Luhnert A, Dennler S, Bloński P, Rusponi S, Etzkorn M, Moulas G, Bencok P, Gambardella P, Brune H, Hafner J (2010) Magnetic anisotropy of Fe and Co ultrathin films deposited on Rh(111) and Pt(111) substrates: An experimental and first-principles investigation, *Phys Rev B*

82:094409.

66. Buschow KHJ, Boer FRD (2003) *Physics of magnetism and magnetic materials*, Kluwer Academic/Plenum publishers New York:92.
67. Wu QS, Zhang YH, Zhou QH, Wang JL, Zeng XC (2018) Transition-Metal dihydride monolayers: A new family of two-dimensional ferromagnetic materials with intrinsic room-temperature half-metallicity. *J. Phys Chem Lett* 9:4260.
68. Guo YL, Zhang YH, Yuan SJ, Wang B, Wang JL (2018) Chromium sulfide halide monolayers: intrinsic ferromagnetic semiconductors with large spin polarization and high carrier mobility. *Nanoscale* 10:18036.
69. Sun YJ, Zhuo ZW, Wu XJ (2018) Bipolar magnetism in a two-dimensional NbS₂ semiconductor with high Curie temperature. *J. Mater. Chem. C* 6:11401.
70. Wang B, Zhang XW, Zhang YH, Yuan SJ, Guo YL, Dong S, Wang JL (2020) Prediction of a two-dimensional high-T_c f-electron ferromagnetic semiconductor. *Materials* 7:1623.
71. Li XX, Yang JL (2019) Realizing two-dimensional magnetic semiconductors with enhanced Curie temperature by antiaromatic Ring based organometallic frameworks. *J. Am. Chem. Soc* 141:109.
72. Hu Y, Liu XY, Shen ZH, Luo ZF, Chen ZG, Fan XL (2020) High Curie temperature and carrier mobility of novel Fe, Co and Ni carbide MXenes. *Nanoscale* 12:11627.
73. Chittari BL, Park YJ, Lee D, Han M, MacDonald AH, Hwang E, Jung J (2016) Electronic and magnetic properties of single-layer MPX₃ metal phosphorous trichalcogenides. *Phys Rev B* 94:184428.
74. Dhoot AS, Israel C, Moya X, Mathur ND, Friend RH (2009) Large electric field effect in electrolyte-gated manganites. *Phys Rev Lett.* 102:136402.
75. Yuan H, Shimotani H, Tsukazaki A, Ohtomo A, Kawasaki M, wasa Y (2009) High-density carrier accumulation in ZnO field-effect transistors gated by electric double layers of ionic liquids. *Adv. Funct. Mater* 19:1046.
76. Jiang SW, Li LZ, Wang ZF, Mak KF, Shan J (2018) Controlling magnetism in 2D CrI₃ by electrostatic doping. *Nat Nanotech* 1:549.

Figures

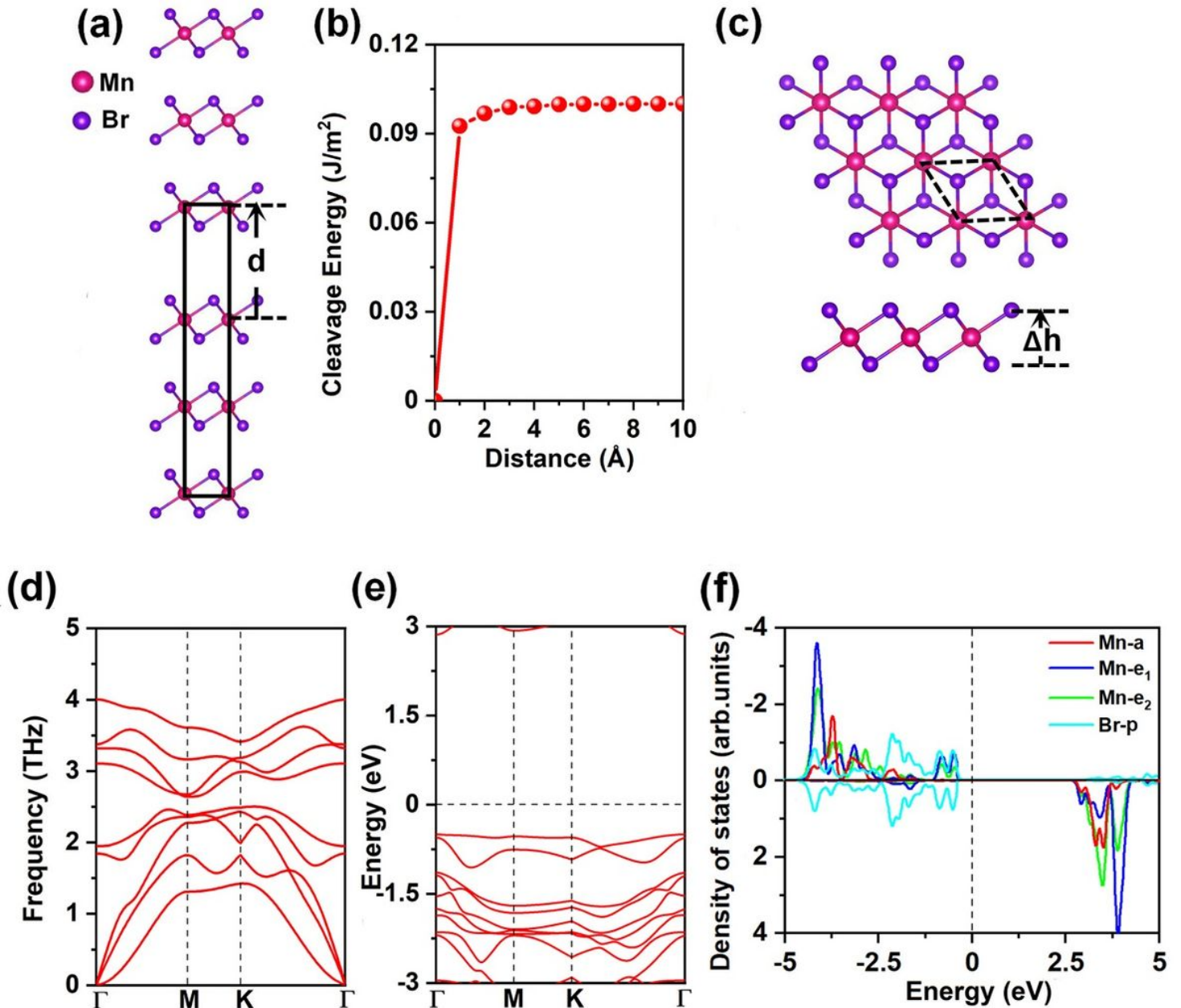


Figure 1

(a) Bulk model of MnBr₂ used to calculate the cleavage energy, and (b) the cleavage energy as a function of the separation between two fractured parts. (c) Top and side views, (d) phonon spectrum, (e) electronic band structure and (f) projected density of states (PDOS) of Mn-d orbitals and Br-p orbitals for MnBr₂ monolayer. represents the vertical distance between two halide planes. The primitive cell is circled in black dashed lines. The Fermi level for band structure and DOS is set as 0eV.

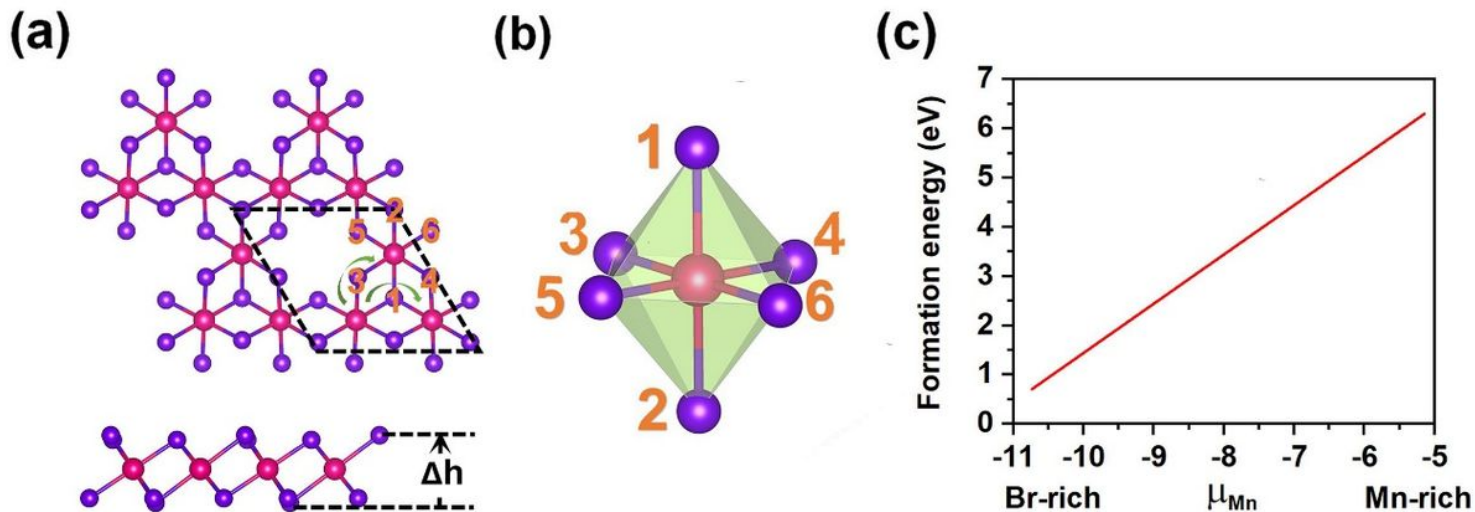


Figure 2

(a) Top and side views for Mn₃Br₈ monolayer, represents the vertical distance between two halide planes. The primitive cell is circulated in black dash lines; the green arrow lines show two different paths of the super-exchange interaction. (b) Structure of the distorted MnBr₆ octahedron. (c) Formation energies for single Mn vacancy as a function of chemical potential of Mn (μ_{Mn}).

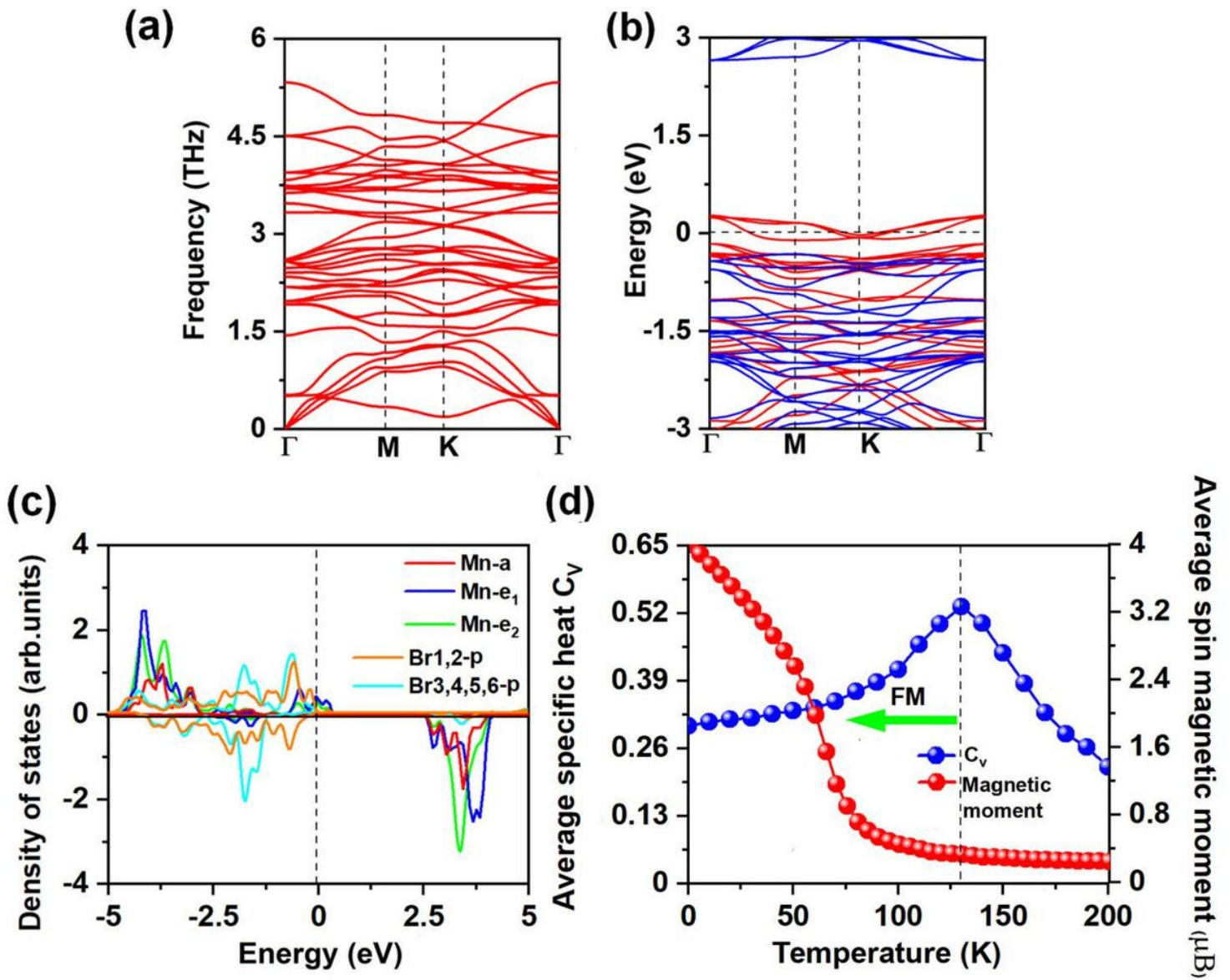


Figure 3

(a) Phonon spectrums, (b) spin-resolved electronic band structure, and (c) projected density of states (PDOS) of Mn-d orbitals and Br-p orbitals for Mn₃Br₈ monolayer. (d) On-site magnetic moments of Mn atoms and the specific heat as function of temperature based on Heisenberg model for Mn₃Br₈ monolayer. The Fermi level for band structure and PDOS is set as 0 eV.

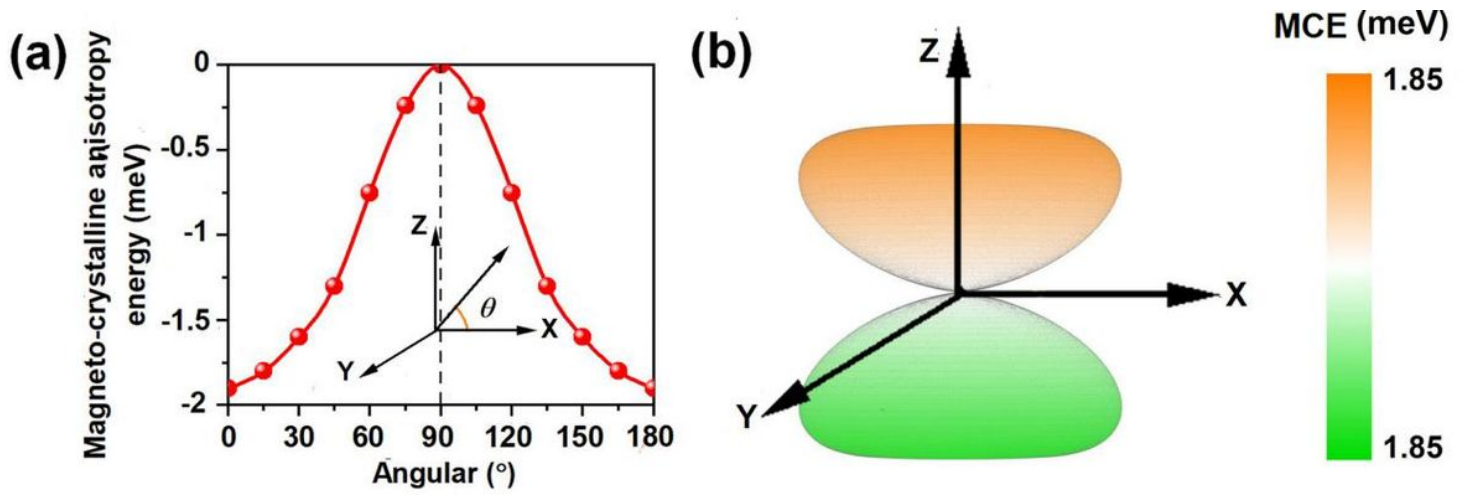


Figure 4

The variation of magneto-crystalline anisotropy energy (MCE) (a) with respect to azimuthal angle and (b) in the space for Mn3Br8 monolayer.

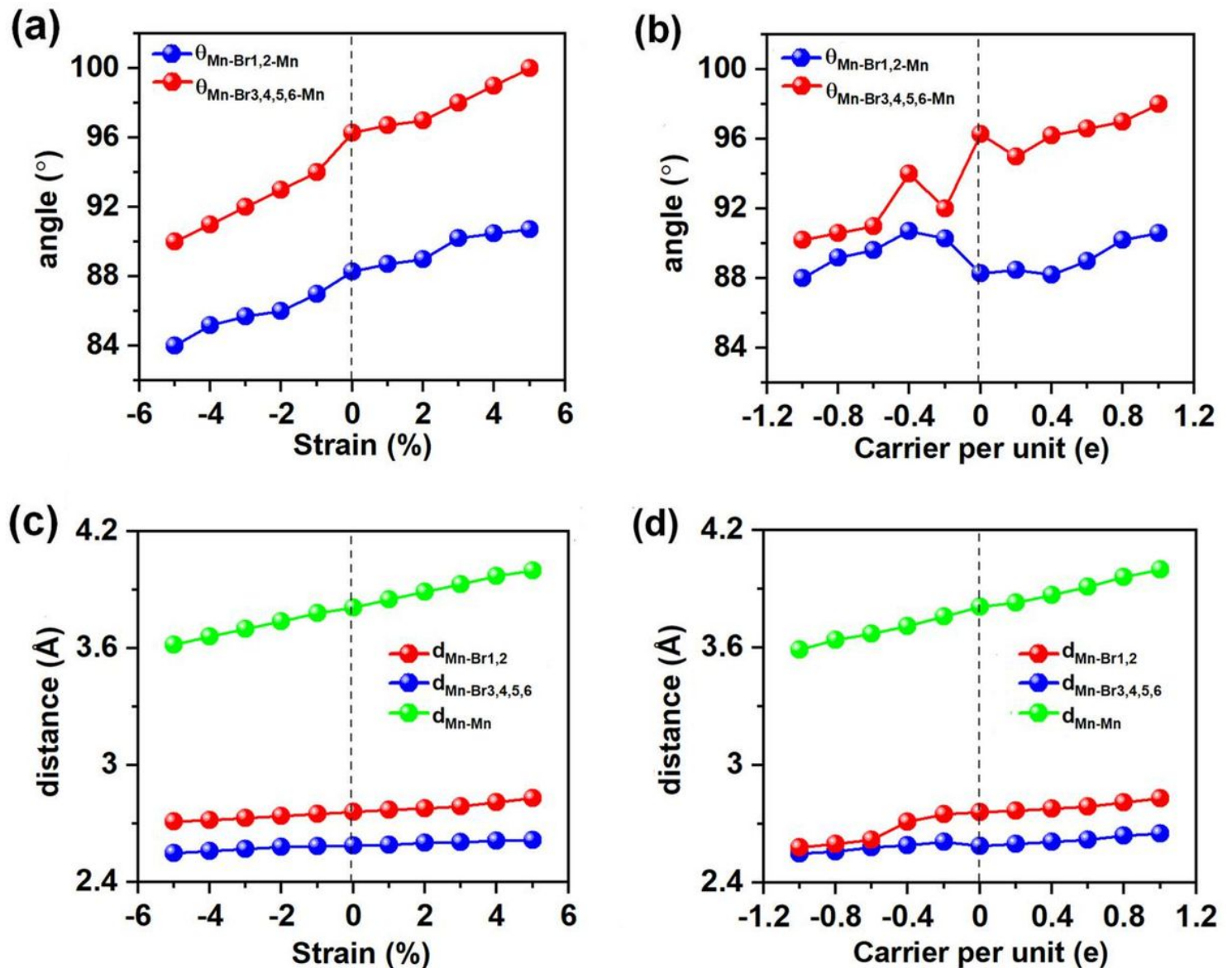


Figure 5

The variations of angles between two Mn and Br atoms, the distance between Mn and Br atoms, and distance between nearest neighboring Mn atoms with respect to the applied biaxial strain and carrier doping. Variation of (a) angle and (c) distance with respect to biaxial strain, variations of (b) angle and (d) distance with respect to carrier doping. Positive and negative values of carrier doping represent the electron and hole doping, respectively.

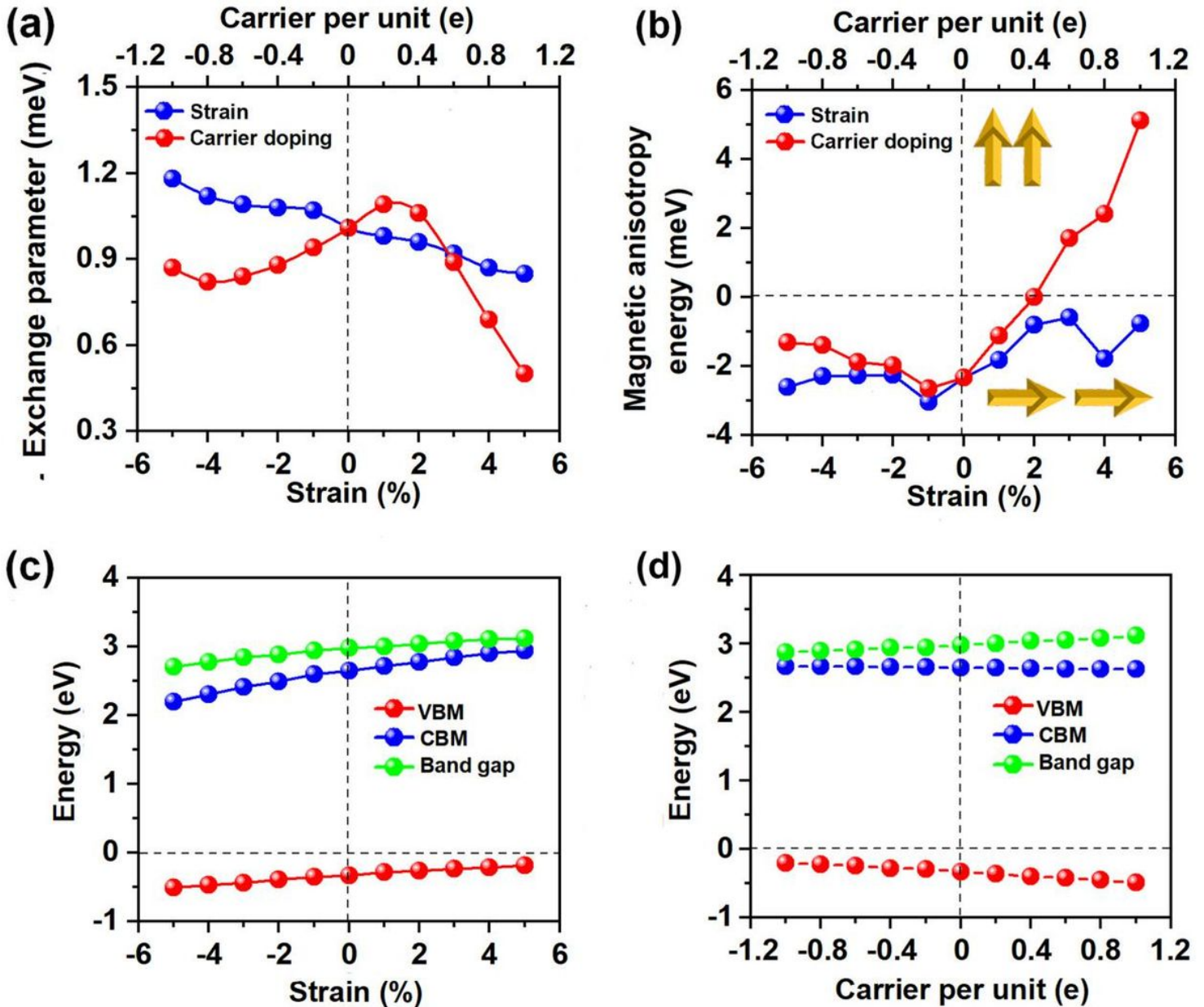


Figure 6

The variations of (a) the exchange parameter and (b) magnetic anisotropy energy (MAE) for Mn₃Br₈ monolayer with respect to the applied biaxial strain and carrier doping. The variations of valence band maximum (VBM), conduction band minimum (CBM) and band gap in the semiconducting channel for

Mn₃Br₈ monolayer with respect to (c) the applied biaxial strain and (d) carrier doping ranging. Positive and negative values of the carrier doping represent the electron and hole doping, respectively.

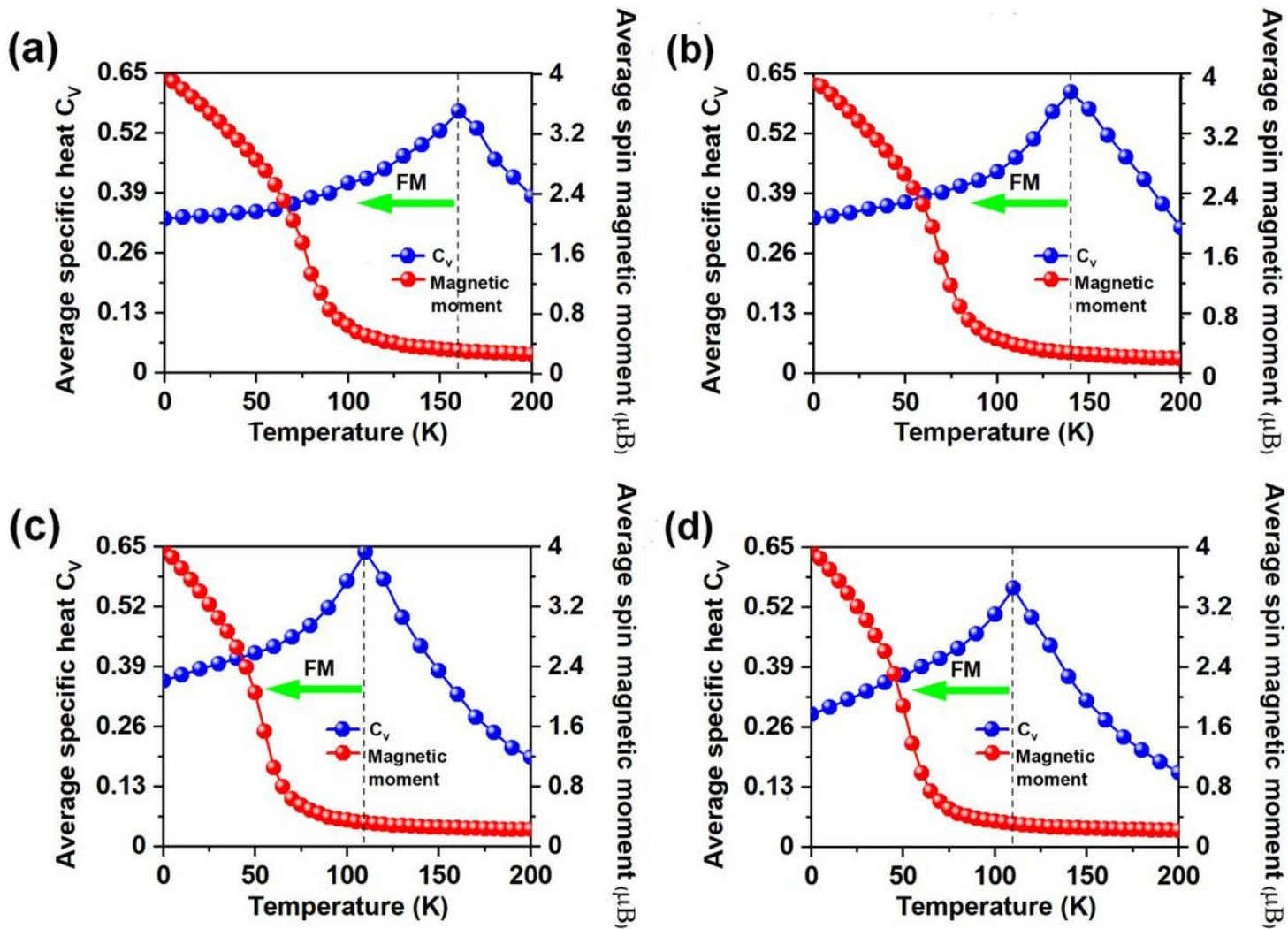


Figure 7

On-site magnetic moments of Mn atoms and the specific heat as function of temperature based on Heisenberg model for Mn₃Br₈ monolayer (a) under -5% biaxial strain, with (b) 0.2e, (c) -0.6e, and (d) -0.8e carrier doping per formula unit. Positive and negative values represent the electron and hole doping, respectively.

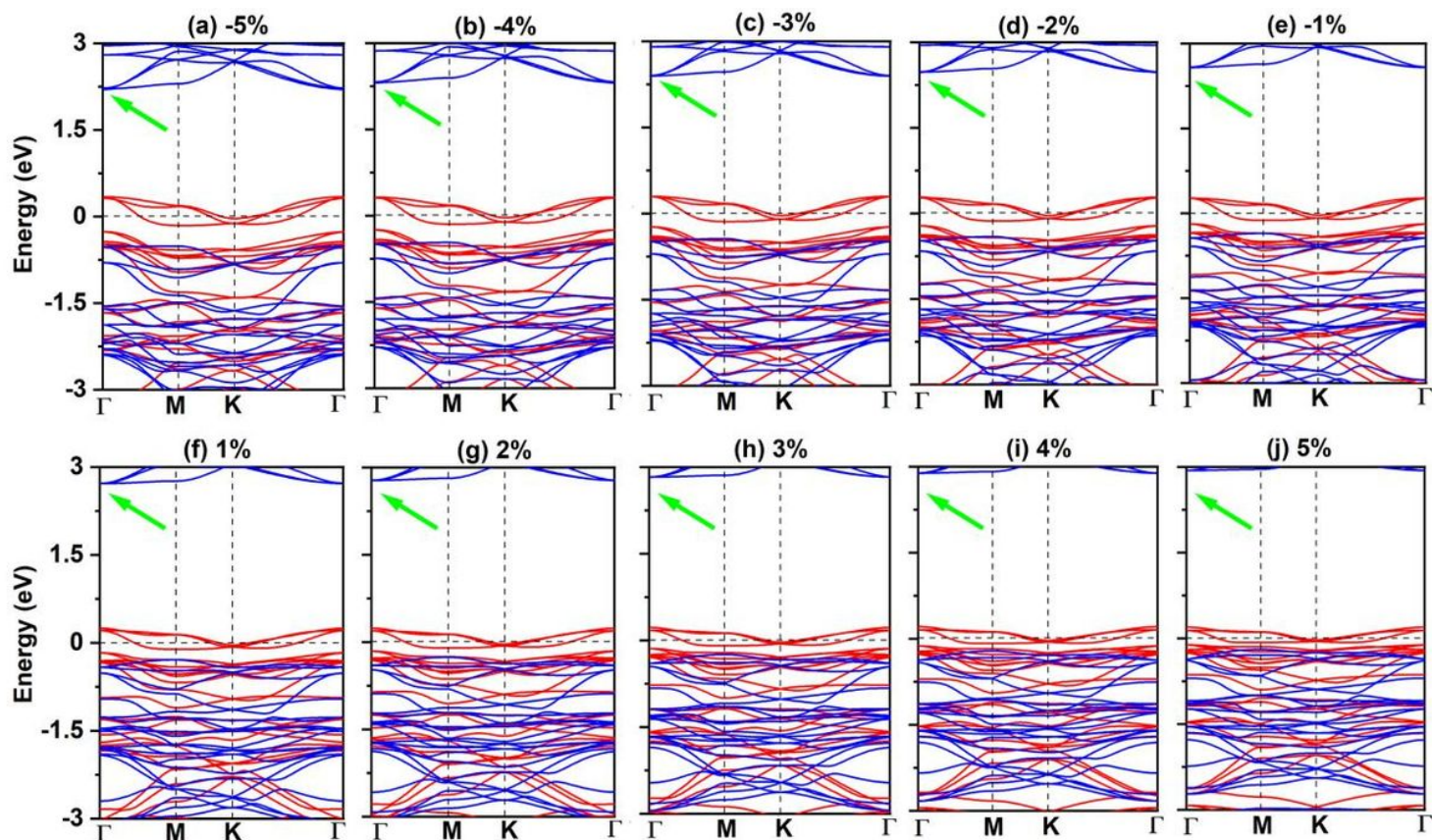


Figure 8

(a)~(j) Spin-resolved band structure for Mn₃Br₈ monolayer under biaxial strain from -5% to 5%.

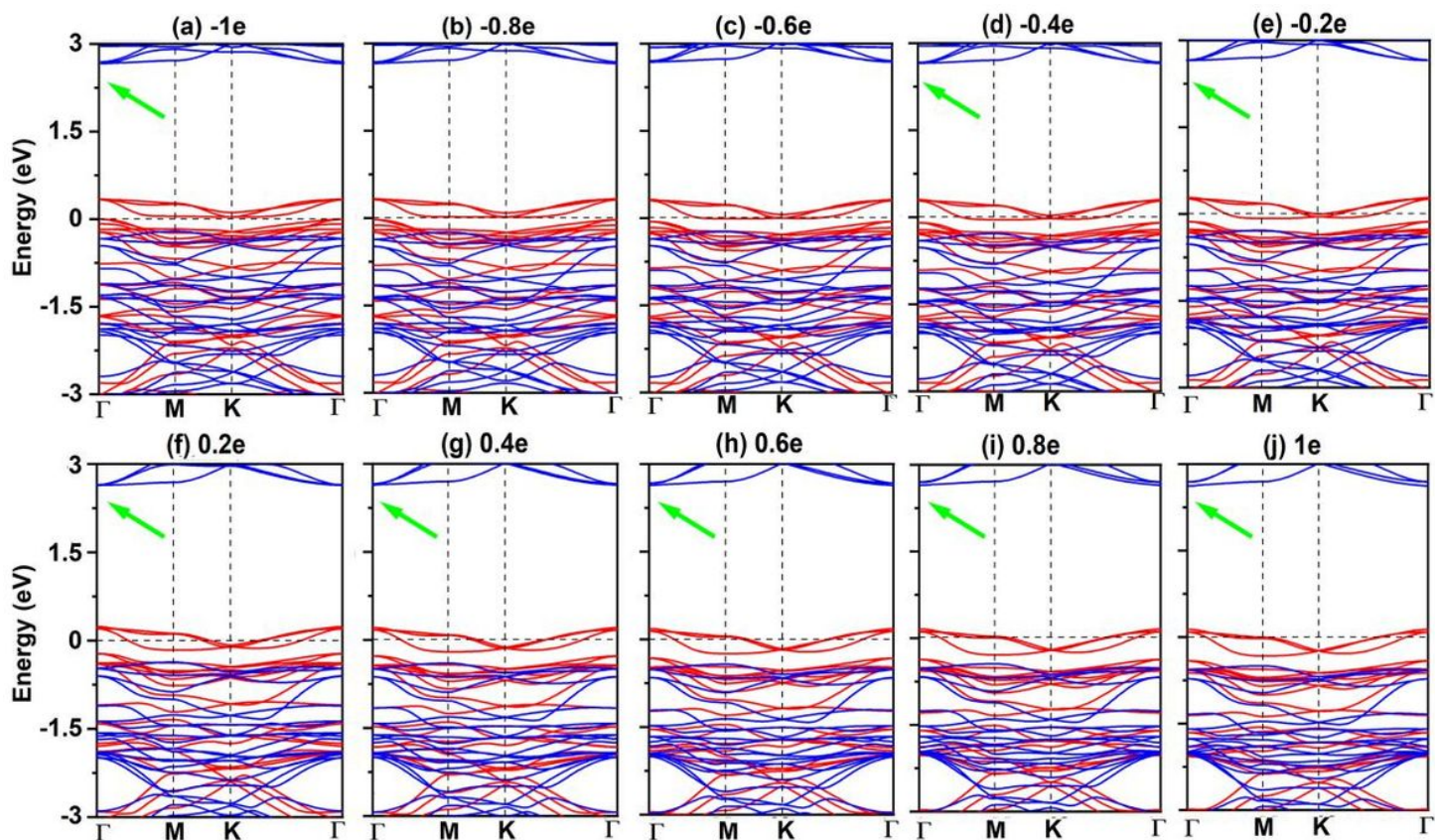


Figure 9

(a)~(j) Spin-resolved band structure for Mn₃Br₈ monolayer with carrier doping from -1e to 1e per formula unit. Positive and negative values represent the electron and hole doping, respectively.

Supplementary Files

This is a list of supplementary files associated with this preprint. Click to download.

- [Sl.docx](#)